

# Analytical Noise Bias Correction for Precise Weak Lensing Shear Inference

Xiangchong Li<sup>1,2\*</sup>, Rachel Mandelbaum<sup>1</sup>, The LSST Dark Energy Science Collaboration

<sup>1</sup> *Department of Physics, McWilliams Center for Cosmology, Carnegie Mellon University, Pittsburgh, PA 15213, USA*

<sup>2</sup> *Brookhaven National Laboratory, Bldg 510, Upton, New York 11973, USA*

Received August 12, 2024; accepted Month ??, 2024

## ABSTRACT

Noise bias is a significant source of systematic error in weak gravitational lensing measurements that must be corrected to satisfy the stringent standards of modern imaging surveys in the era of precision cosmology. This paper reviews the analytical noise bias correction method and provides analytical derivations demonstrating that we can recover shear to its second order using the “renoising” noise bias correction approach introduced by `METACALIBRATION`. We implement this analytical noise bias correction within the `AnaCa1` shear estimation framework and propose several enhancements to the noise bias correction algorithm. We evaluate the improved `AnaCa1` using simulations designed to replicate Rubin LSST imaging data. These simulations feature semi-realistic galaxies and stars, complete with representative distributions of magnitudes and Galactic spatial density. We conduct tests under various observational challenges, including cosmic rays, defective CCD columns, bright star saturation, bleed trails, and spatially variable point spread functions. Our results indicate a multiplicative bias in weak lensing shear recovery of less than a few tenths of a percent, meeting LSST DESC requirements without requiring calibration from external image simulations. Additionally, our algorithm achieves rapid processing, handling one galaxy in less than a millisecond.

**Key words:** gravitational lensing; weak; cosmology; observations; techniques; image processing.

## 1 INTRODUCTION

We are now entering the era of precision cosmology, marked by the initiation of groundbreaking astronomical imaging surveys. These surveys will provide precise tests of the current cosmological paradigm, including understanding the accelerated expansion rate of the Universe using measurements of cosmic structure growth with weak gravitational lensing. Gravitational lensing occurs when the gravity of massive structures in the Universe bends the light from distant galaxies, resulting in coherent distortions in the images of these galaxies (Bartelmann & Schneider 2001; Kilbinger 2015; Mandelbaum 2018). Prominent among these advanced “stage IV” imaging surveys are the Vera C. Rubin Observatory Legacy Survey of Space and Time (LSST, Ivezić et al. 2019), the Euclid mission (Laureijs et al. 2011), and studies using the Nancy Grace Roman Space Telescope (Spergel et al. 2015; Akeson et al. 2019). These imaging surveys require shear measurement techniques that achieve precision within a few tenths of a percent (Massey et al. 2013; The LSST Dark Energy Science Collaboration et al. 2018) to meet their ambitious objectives. The deployment of such sophisticated algorithms necessitates tailored approaches to effectively process and analyze the data collected by each specific survey.

Several shear measurement techniques have shown promise

in meeting the stringent requirements for analyzing noisy, “blended” galaxy images with a constant applied shear, without the need for calibration through external image simulations. These methods include `METADTECTION` (Sheldon et al. 2020, 2023), a numerical self-calibration method; and `AnaCa1` (Li & Mandelbaum 2023; Li et al. 2024), an analytical framework designed to derive linear shear response. Of these two, `AnaCa1` stands out as the most efficient due to its analytical nature — it takes  $< 1$  millisecond to compute the shear estimator for one detected galaxy. Another promising technique is `BFD` (Bernstein & Armstrong 2014; Bernstein et al. 2016), a Bayesian approach to shear estimation. However, as of the current writing, it still necessitates additional percent-level correction, based on simulations, to address detection biases due to blending. We acknowledge that external image simulations may be required to calibrate the redshift distribution of source galaxies in cases where blending occurs between galaxies at different redshifts, each subject to distinct shear distortions (MacCrann et al. 2022). In this paper, we focus on analytically correcting shear estimation bias under a constant shear scenario, and defer the discussion of blending effects across varying redshifts to future work.

Li & Mandelbaum (2023) developed an analytical formalism that effectively corrects both detection bias and shear estimation bias. This approach, accurate to second order in shear, operates independent of the specific details of galaxy morphologies. The method defines the detection pro-

\* xli6@bnl.gov

cess through a series of step functions based on several basic linear observables. These basic observables were chosen for their property of having analytically solvable linear shear responses. By utilizing the shear responses of these basic observables, Li & Mandelbaum (2023) were able to calculate the linear shear response of the detection process using the chain rule. The formalism has been applied to the FPFS shear estimator (Li et al. 2018, 2022b), a fixed-kernel method for measuring galaxy shapes, which constructs shapes as nonlinear functions of shapelet modes. These shapelet modes are obtained by projecting the galaxy image onto a shapelet basis. We refer readers to Refregier (2003); Massey & Refregier (2005); Bernstein & Jarvis (2002) for details of shapelet basis functions. The shear response of the galaxy shape is then derived using the chain rule, based on the pre-calculated shear responses of the shapelet modes.

In Li & Mandelbaum (2023), a perturbation approach, as outlined in Kaiser (2000), was employed to correct for noise bias in shear estimation. This method uses the Hessian matrix (which can be fully calculated using JAX (Bradbury et al. 2018) following Li et al. 2024) of the nonlinear ellipticity, which is defined as a function of basic modes, including shapelet and peak detection modes. However, this approach necessitates the use of step functions with very gentle transition for galaxy selection and detection to maintain stability in the Hessian matrix. Consequently, the precision of the shear estimation is compromised and remains suboptimal since it causes “ambiguous” detections near the galaxy peaks. In this paper, we will explore an alternative method for correcting noise bias, as proposed by Huff & Mandelbaum (2017); Sheldon & Huff (2017), which involves adding noise to galaxy images. We will adapt this approach within the AnaCal framework, providing a rigorous analytical proof and introducing several extensions to the methodology. Although this method internally introduces additional noise to the images, it proves to be more effective than the perturbation approach to noise bias correction. This effectiveness stems from its capability to incorporate multiple layers of differentiable selection cuts without requiring the calculation of the noisy Hessian matrix. This approach not only enhances galaxy detection but also improves the precision of shear estimation.

Furthermore, in this paper, we will demonstrate that the AnaCal shear estimator effectively calibrates shear estimates using data that closely resembles the calibrated LSST coadded images. We generate simulated images incorporating galaxies and stars, reflecting realistic galactic density distributions, spatially variable point spread functions (PSF), and proxies for image artifacts, using the Dark Energy Science Collaboration (DESC) weak lensing simulation package<sup>1</sup> (Sheldon et al. 2023). In this paper, our focus is on evaluating the shear estimation technique using well-calibrated data without errors on the PSF model and the astrometric and photometric calibrations, and where the statistics of the image noise are perfectly known. However, in practical data analyses, calibration inaccuracies can substantially contribute to systematic errors in shear measurements. It is important to note that the accuracy of shear measurements may be more dependent on the quality of data characterization than on the estimation technique itself.

<sup>1</sup> <https://github.com/LSSTDESC/descwl-shear-sims>

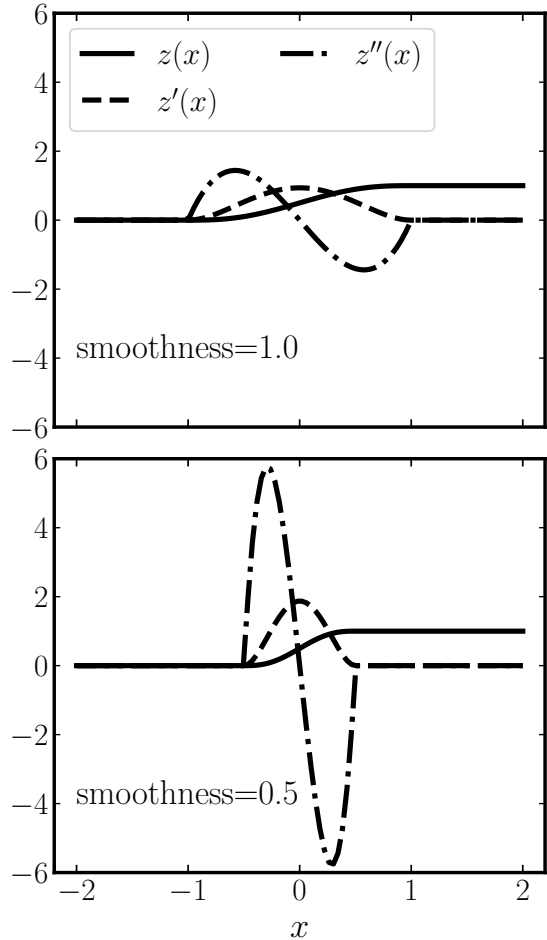


**Figure 1.** Smoothstep functions with two smoothness parameters (1 for the upper panel and 0.5 for the lower panel) used to select and detect galaxies and their derivatives. The step functions ( $z(x)$ ) are shown with solid lines; the first ( $z'(x)$ ) and second-order ( $z''(x)$ ) derivatives of the functions are in dashed lines and dotted-dashed lines.

This paper is organized as follows: Section 2 reviews the shear estimator and introduces a new analytical noise bias correction scheme. Section 3 presents systematic tests of LSST-like image simulations under various conditions. Finally, Section 4 provides a summary and outlook.

## 2 ANALYTICAL SHEAR ESTIMATION

In this section, we begin by reviewing the derivation of the shear response for the FPFS shear estimator, which has been calibrated using the AnaCal framework (see Section 2.1). Following this, we explore the derivation of the shear response from noisy data, employing two distinct methodologies (see Section 2.2). The procedure of our image processing pipeline is detailed in Appendix A.

## 2.1 Observables and Shear Responses

We follow Li & Mandelbaum (2023) to use a set of linear observables that are linear combinations of pixel values to define the galaxy shape, size flux and detection process. The linear observables include shapelet modes (Refregier 2003; Massey & Refregier 2005) and detection modes (Li & Mandelbaum 2023). The vector of linear observables are denoted as  $\boldsymbol{\nu} = (\nu_1, \nu_2, \dots, \nu_n)$ , and we follow the notation in Li et al. (2022b) —  $\bar{\boldsymbol{\nu}}$ ,  $\boldsymbol{\nu}$  and  $\tilde{\boldsymbol{\nu}}$  are the prelensed, lensed noiseless and lensed noisy observables, respectively. Additionally, we use a double tilde ( $\tilde{\tilde{\boldsymbol{\nu}}}$ ) to denote linear observables with doubled image noise. We note that these linear observables are projection of image onto basis kernels after PSF deconvolution in Fourier space (Zhang 2008). Denoting the basis kernels as  $\chi_i(\mathbf{k})$ , PSF as  $p(\mathbf{k})$  and galaxy image as  $f(\mathbf{k})$ , we have

$$\nu_i = \int_{\mathbf{k}} f(\mathbf{k}) \frac{\chi_i(\mathbf{k})}{p(\mathbf{k})}. \quad (1)$$

$\chi_i$  can be any function as long as  $\int_{\mathbf{k}} \frac{\chi_i(\mathbf{k})}{p(\mathbf{k})}$  is finite. In this paper, we use  $\int_{\mathbf{k}} \equiv \int d\mathbf{k}$  to indicate integration over the  $\mathbf{k}$  space. In addition, this notation of integration applies to any quantities (e.g.,  $\boldsymbol{\nu}$ ).

The basis kernels are composed of polar shapelets and peak detection basis. Polar shapelets (Massey & Refregier 2005), which are used as basis functions, are defined in polar coordinates  $(\rho, \theta)$  as

$$\begin{aligned} \phi_{nm}(\mathbf{x} | \sigma_h) &= (-1)^{(n-|m|)/2} \left\{ \frac{[(n-|m|)/2]!}{[(n+|m|)/2]!} \right\}^{\frac{1}{2}} \\ &\times \left( \frac{\rho}{\sigma_h} \right)^{|m|} L_{\frac{n-|m|}{2}}^{|m|} \left( \frac{\rho^2}{\sigma_h^2} \right) e^{-\rho^2/2\sigma_h^2} e^{im\theta}, \end{aligned} \quad (2)$$

where  $L_{\frac{n-|m|}{2}}^{|m|}$  are the Laguerre polynomials,  $n$  is the radial number, which can be any non-negative integer, and  $m$  is the spin number, which is an integer between  $-n$  and  $n$  in steps of two.  $\sigma_h$  determines the scale of shapelet functions, which is set to 0.52 to maximize the effective galaxy number density according to Li et al. (2024). Additionally, the peak detection basis functions for the peak detection modes are

$$\psi_i = \frac{1}{(2\pi)^2} e^{-|\mathbf{k}|^2 \sigma_h^2 / 2} \left( 1 - e^{i(k_1 x_i + k_2 y_i)} \right), \quad (3)$$

where  $(x_i, y_i) = (\cos(i\pi/2), \sin(i\pi/2))$ , and  $i = 0, 1, 2, 3$ . The origin reference point for the measurements of the linear observables is set at the preselected ‘‘peak candidates’’ (Li & Mandelbaum 2023).

To focus on shear estimation, in this paper, we set the lensing convergence to zero and ignore the distinction between shear and reduced shear. Given that the lensing shear distortion is small within the weak lensing regime, it is a practical approach to employ a first-order approximation to understand the transformation of observables under shear distortion. The linear observables were chosen due to their advantageous properties, notably that they have analytically solvable linear shear responses. Specifically, under lensing shear distortion, the linear observables transform as

$$\boldsymbol{\nu} = (\bar{\boldsymbol{\nu}} + \gamma_1 \boldsymbol{\nu}_{;1} + \gamma_2 \boldsymbol{\nu}_{;2}) + \mathcal{O}(\gamma^2), \quad (4)$$

where  $\boldsymbol{\nu}_{;1}$  and  $\boldsymbol{\nu}_{;2}$  are the linear shear response with respect

to the first and second components of the lensing shear distortion:

$$\boldsymbol{\nu}_{;1} \equiv \frac{\partial \boldsymbol{\nu}}{\partial \gamma_1}, \quad \boldsymbol{\nu}_{;2} \equiv \frac{\partial \boldsymbol{\nu}}{\partial \gamma_2}. \quad (5)$$

The  $i$ th components of the linear shear responses with respect to two shear components are denoted as  $\nu_{;1i}$  and  $\nu_{;2i}$ . These observables are the projection of the deconvolved image onto the shear response of the corresponding basis functions (Li & Mandelbaum 2023), denoted as  $\chi_{;1i}(\mathbf{k})$  and  $\chi_{;2i}(\mathbf{k})$  for the two shear components:

$$\nu_{;1i} = \int_{\mathbf{k}} f(\mathbf{k}) \frac{\chi_{;1i}(\mathbf{k})}{p(\mathbf{k})}, \quad \nu_{;2i} = \int_{\mathbf{k}} f(\mathbf{k}) \frac{\chi_{;2i}(\mathbf{k})}{p(\mathbf{k})}. \quad (6)$$

More specifically, the shapelet basis set is closed under the shear perturbation operation. As a result, the shear response of any shapelet basis can be written as a combination of shapelet basis (Bernstein & Jarvis 2002). The shear responses of the peak detection basis functions are given by Li & Mandelbaum (2023):

$$\begin{aligned} \psi_{;1i} &= \frac{1}{(2\pi)^2} e^{-|\mathbf{k}|^2 \sigma_h^2 / 2} (k_1^2 - k_2^2) \sigma_h^2 \left( 1 - e^{i(k_1 x_i + k_2 y_i)} \right) \\ &\quad - \frac{1}{(2\pi)^2} e^{-|\mathbf{k}|^2 \sigma_h^2 / 2} (ix_i k_1 - iy_i k_2) e^{i(k_1 x_i + k_2 y_i)}, \\ \psi_{;2i} &= \frac{1}{(2\pi)^2} e^{-|\mathbf{k}|^2 \sigma_h^2 / 2} (2k_1 k_2) \sigma_h^2 \left( 1 - e^{i(k_1 x_i + k_2 y_i)} \right) \\ &\quad - \frac{1}{(2\pi)^2} e^{-|\mathbf{k}|^2 \sigma_h^2 / 2} (iy_i k_1 + ix_i k_2) e^{i(k_1 x_i + k_2 y_i)}. \end{aligned} \quad (7)$$

Nonlinear observables  $e_{1,2}$  are defined as nonlinear functions of the linear observables  $\boldsymbol{\nu}$ :

$$e_{1,2}(\boldsymbol{\nu}) = \epsilon_{1,2}(\boldsymbol{\nu}) w_s(\boldsymbol{\nu}) w_d(\boldsymbol{\nu}), \quad (8)$$

where  $\epsilon_{1,2}$  is the spin-2 FPFS ellipticity defined in Li et al. (2018) measuring galaxy shape.  $w_s$  represents the selection weight, while  $w_d$  denotes the detection weight (Li & Mandelbaum 2023). They serve the purposes of galaxy sample selection and galaxy detection, respectively. These weights are formulated using smoothstep functions of the linear observables (Li & Mandelbaum 2023). To elaborate, if the weight for a galaxy is set to zero, it implies rejection from the sample. The smoothstep functions for a cut at zero are demonstrated in Figure 1. Since our detection operation, defined with the smoothstep function, is differentiable, the reference points change smoothly in response to shear distortion. This allows us to quantify the changes in the population of these reference points through their shear response. Specifically, under shear distortion, some reference points may disappear (with their weight transitioning from non-zero to zero), while others may reappear (with their weight transitioning from zero to non-zero).

Specifically, the FPFS ellipticity in equation (8) is defined as

$$\epsilon_1 + i\epsilon_2 \equiv \frac{M_{22}}{M_{00} + C}, \quad (9)$$

where the shapelet modes  $M_{nm}$  are the linear observables obtained by projecting (see equation (1)) the image onto deconvolved polar shapelet functions defined in equation (2). For further details on polar shapelet functions, we refer readers to Bernstein & Jarvis (2002); Massey & Refregier (2005). The weighting parameter  $C$ , introduced by Li et al. (2018), is a constant specific to a galaxy sample. By adjusting the value

of  $C$ , one can change the relative weights assigned to galaxies of different brightnesses within the sample. The selection weight in equation (8) has two components — selection on signal-to-noise ratio (SNR) denoted as  $w_0$  and selection on galaxy size denoted as  $w_2$ :

$$w_s = w_0 w_2. \quad (10)$$

The differentiable selection weight with minimal SNR equals  $s_{\min}$  is

$$w_0 = z_{\Omega_0} \left( \frac{M_{00}}{\sigma_0} - s_{\min} \right), \quad (11)$$

where  $\sigma_0$  is the standard deviation of measurement error due to image noise on the zeroth order shapelet mode  $M_{00}$ . In addition, the differentiable selection weight with minimal galaxy size  $r_{\min}$  is

$$w_2 = z_{\Omega_2} (M_{20} + (1 - r_{\min})M_{00}). \quad (12)$$

$z_{\Omega}$  is smoothstep function (Hazimeh et al. 2020) with smoothness parameter equals  $\Omega$  (see Figure 1):

$$z_{\Omega}(x) = 6 \left( \frac{x + \Omega}{2\Omega} \right)^5 - 15 \left( \frac{x + \Omega}{2\Omega} \right)^4 + 10 \left( \frac{x + \Omega}{2\Omega} \right)^3, \quad (13)$$

where  $x \in [-\Omega, \Omega]$ . The smoothstep function equals zero for  $x < -\Omega$ , and 1 for  $x > \Omega$ . In this paper, we adopt two detection layers. To be more specific, the detection weight is defined as

$$w_d = z_{\Omega_d}(w_q - w_{\min}), \quad (14)$$

where  $z_{\Omega_d}$  is the second detection layer, and the first detection layer is similar to Li & Mandelbaum (2023):

$$w_q = \prod_{i=0}^3 z_{\Omega_q}(q_i - q_{\min}), \quad (15)$$

where  $q_{\min} = \Omega_q - 0.8\sigma_q$ .  $q_i$  ( $i = 0 \dots 3$ ) are the four peak detection modes measuring the difference between neighboring four pixels after smoothing, and  $\sigma_q$  is the standard deviation of measurement error on the peak detection modes.  $q_i$  is obtained by projecting the image onto deconvolved detection basis functions (Li & Mandelbaum 2023). The second detection layer performs differentiable smooth selection on the output detection weight from the first layer to reduce the number of subpeaks near the galaxy centers. The default hyper parameters are set to  $C = 4\sigma_0$ ,  $\Omega_0 = \Omega_2 = 1.6\sigma_0$ ,  $\Omega_q = 1.6\sigma_q$ ,  $\Omega_d = 0.04$ ,  $s_{\min} = 12$ ,  $r_{\min} = 0.1$ ,  $w_{\min} = 0.12$ . These hyperparameters are fine-tuned to optimize the effective galaxy number density using image simulations. We have confirmed that the accuracy remains robust even when the parameters are varied slightly around their optimal values. We refer readers to Li et al. (2024) for more details on how to optimize the effective galaxy number density.

Before presenting the linear shear response of the weighted ellipticity  $e_{1,2}$ , we conduct a spin analysis to justify that the first order approximation is accurate to the second order of shear due to the rotational symmetry. Initially, we note that the galaxy ellipticity  $\epsilon_{1,2}$  is inherently a spin-2 quantity so that it negates under a  $90^\circ$  rotation. The selection and detection weights are specifically designed to remain invariant under a  $90^\circ$  rotation, as outlined by Li & Mandelbaum (2023). As a result, the weighted ellipticity reverses sign under a  $90^\circ$  rotation indicating the absence of both spin-0 and spin-4 components. Assuming that the intrinsic galaxies are isotropically

oriented and their positions are randomly distributed prior to shear distortion, since the weighted ellipticity lacks spin-0 components, we have

$$\langle e_{1,2} |_{\gamma=0} \rangle_g = 0, \quad (16)$$

where  $\langle \cdot \rangle_g$  is the average over galaxy population. Additionally, since the weighted ellipticity lacks both spin-0 and spin-4 components, we have

$$\left\langle \frac{\partial^2 e_{1,2}}{\partial \gamma_i \partial \gamma_j} \Big|_{\gamma=0} \right\rangle_g = 0, \quad (17)$$

where  $i, j \in \{1, 2\}$  (see Appendix A of Li & Mandelbaum 2023). Furthermore, from equation (17), we derive

$$\left\langle \frac{\partial e_i}{\partial \gamma_j} \right\rangle = \left\langle \frac{\partial e_i}{\partial \gamma_j} \Big|_{\gamma=0} \right\rangle_g + \mathcal{O}(\gamma^2), \quad (18)$$

indicating that we can directly assess the shear response to the first order in shear from the distorted image without reverting to the intrinsic image before shear distortion. The bias introduced by this estimation of the shear response is at the second-order of shear. Therefore, the expectation value of the weighted ellipticity under the lensing shear distortion can be derived with a Taylor expansion and omitting the zeroth order and the second-order terms since their expectation values are zero:

$$\langle e_i \rangle = \sum_{j=1}^2 \left\langle \frac{\partial e_i}{\partial \gamma_j} \right\rangle_g \gamma_j + \mathcal{O}(\gamma^3), \quad (19)$$

where  $i = 1, 2$ . We observe that equation (19) remains accurate up to the second order of shear, as the expectation value of the weighted ellipticity's second-order derivatives with respect to shear is zero. For more details, we refer readers to Li & Mandelbaum (2023).

The linear shear response matrix,  $\frac{\partial e_i}{\partial \gamma_j}$ , where  $j = 1, 2$ , can be expressed with the linear shear response of the linear observables using the chain rule:

$$\frac{\partial e_i}{\partial \gamma_j} = \sum_k \frac{\partial e_i}{\partial \nu_k} \frac{\partial \nu_k}{\partial \gamma_j} = \sum_k \frac{\partial e_i}{\partial \nu_k} \nu_{:jk}, \quad (20)$$

where  $\nu_{:jk}$  is the  $k$ th component of the shear response vector  $\nu_{:j}$ .

In the following subsections, we will derive the shear response for the first component of ellipticity for noisy data. The methodology for the second component follows the same approach and can be derived accordingly.

## 2.2 Estimating Shear Response From Noisy Data

In real observations, there is noise in the images, causing measurement error. We denote the measurement error on the linear observable vector as  $\delta \nu$ , and we have

$$\delta \nu_i = \int_{\mathbf{k}} n(\mathbf{k}) \frac{\chi_i(\mathbf{k})}{p(\mathbf{k})}, \quad (21)$$

where  $n(\mathbf{k})$  is the pure noise image in Fourier space, and the integration is over the 2D Fourier space. The nonlinear function  $e_1$  is calculated on the noisy linear observables  $\tilde{e}_1 = e_1(\tilde{\nu})$ , where  $\tilde{\nu} = \nu + \delta \nu$ . The noise is described by its probability density function (PDF)  $P_n(\delta \nu)$ . We focus on

the condition that the sky background is precisely subtracted such that the sum of the noise PDF equals one and it possesses a zero mean:

$$\int_{\delta\nu} P_n(\delta\nu) = 1, \quad \int_{\delta\nu} \delta\nu_i P_n(\delta\nu) = 0. \quad (22)$$

where  $\nu_i$  is the  $i$ th element of the linear observable vector, and the integration on the noise realization over the space defined with the states of the image noise. Furthermore, in the derivation, we assume that the image noise is homogeneous and additive, which is a reasonable approximation for faint, small galaxies observed in ground-based surveys because the main source of noise comes from fluctuations in the sky background. However, it is important to note that this assumption does not hold in practical scenarios when interpolating over bad pixels, cosmic rays, etc. As discussed in Section 3.7, we address this by masking pixels with artifacts prior to detection and shear estimation.

The average ellipticity measured from noisy data is

$$\langle \tilde{e}_1 \rangle = \int_{\nu} P_g(\nu) \int_{\delta\nu} e_1(\nu + \delta\nu) P_n(\delta\nu), \quad (23)$$

where  $P_g(\nu)$  is the galaxy PDF after the lensing effect. Due to the invariance of the probability measure — the probability of the random variable falling within a particular volume before and after the transformation should be the same — we have  $P_g(\nu) d\nu = \bar{P}_g(\bar{\nu}) d\bar{\nu}$ , where  $\bar{P}_g$  is the PDF before lensing shear distortion. In this paper, PDFs with bar refer to those before the lensing shear distortion. Additionally,  $\langle \cdot \rangle$  is the average over galaxy population and noise realizations.

We note that due to the nonlinearity in ellipticity, the average galaxy ellipticity over different noise realizations is biased compared to the noiseless estimation:

$$\int_{\delta\nu} e_1(\nu + \delta\nu) P_n(\delta\nu) \neq e_1(\nu), \quad (24)$$

and the corresponding bias in shear estimation is termed noise bias (Refregier et al. 2012). Without any noise bias correction, our shear estimation exhibits a multiplicative bias of a few percent, which is approximately ten times higher than the subpercent-level requirement set by the LSST DESC.

In the following context of this subsection, we outline two distinct analytical approaches for noise bias correction. These methodologies do not make any assumption on galaxy morphology and do not rely on simulated images. The first approach involves correcting the noise bias in the ensemble average of the noisy ellipticity, transforming it back to that expected for the noiseless ellipticity, which is then used for shear measurement (Section 2.2.1). The second approach directly estimates the shear response based on the expectation value of the noisy ellipticity (Section 2.2.2).

### 2.2.1 Noise Correction Approaches

This methodology draws its inspiration from the foundational work of Kaiser (2000), and has been refined in Li et al. (2022b) and Li & Mandelbaum (2023). Specifically, we compute the Taylor expansion of the noisy ellipticity as a function of  $\delta\nu$ , offering a derivation of shear bias to 2nd order in image noise:

$$e_1(\nu + \delta\nu) = e_1(\nu) + \frac{\partial e_1(\nu)}{\partial \nu_i} \delta\nu_i + \frac{1}{2} \frac{\partial^2 e_1(\nu)}{\partial \nu_i \partial \nu_j} \delta\nu_i \delta\nu_j + \mathcal{O}(\delta\nu^3). \quad (25)$$

We direct readers to equation (21) of Li et al. (2022b) for a detailed application of this noise bias correction method. Here we employ Einstein notation, wherein repeated indices imply summation over those indices. We substitute equation (25) into equation (23) and the expectation value of the noisy ellipticity is

$$\langle \tilde{e}_1 \rangle = \langle e_1 \rangle + \frac{1}{2} \left\langle \frac{\partial^2 e_1(\nu)}{\partial \nu_i \partial \nu_j} \right\rangle_g \langle \delta\nu_i \delta\nu_j \rangle_n + \mathcal{O}(\delta\nu^3), \quad (26)$$

where  $\langle \cdot \rangle_g$  is the average over lensed noiseless galaxy population (operation  $\int_{\nu} P_g(\nu)[\cdot]$ ); whereas  $\langle \cdot \rangle_n$  is the average over noise realizations (operation  $\int_{\delta\nu} P_n(\delta\nu)[\cdot]$ ).  $\langle \delta\nu_i \delta\nu_j \rangle_n$  is the covariance matrix of measurement error on the linear observables that are given in Li & Mandelbaum (2023). We note that the above derivation assumes the realization of the image noise (the value of the image noise) is independent of the specifics of the galaxy's surface brightness profile. This assumption holds true for ground-based surveys that are dominated by sky background. However, it is not valid in space-based observations which are dominated by source Poisson noise, where the variance of the image noise is dependent on the expectation of the pixel value. Another source of image noise is readout noise from the detector. When the readout noise is homogeneous across the measurement scale (as defined by the shapelet kernel), this correction scheme can be applied to mitigate noise bias. While additional calibration may be required to address any inhomogeneity in the noise distribution, such considerations are beyond the scope of this paper.

The corrected expectation value of ellipticity  $\langle e \rangle$  is distorted by the lensing shear, and it is related to the PDF of the galaxy population before shearing:

$$\langle e_1 \rangle = \int_{\nu} P_g(\nu) e_1(\nu) = \int_{\bar{\nu}} \bar{P}_g(\bar{\nu}) e_1(T(\bar{\nu})), \quad (27)$$

where  $\bar{P}_g$  is the PDF of galaxy population before the shear distortion, and  $T$  is the mapping from the intrinsic linear observables  $\bar{\nu}$  to the lensed linear observables  $\nu$ . Following equation (20), the linear shear response at the single galaxy level can be written as a function of linear observables

$$R_1(\nu) = \frac{\partial e_1(\nu)}{\partial \nu_i} \frac{\partial \nu_i}{\partial \gamma_1} = \frac{\partial e_1(\nu)}{\partial \nu_i} \nu_{;1i}. \quad (28)$$

Here, we present only the diagonal term of the linear shear response matrix, as the expectation value of the off-diagonal terms is zero (Li & Mandelbaum 2023). When dealing with noisy data, we first measure the expectation of the noisy shear response  $\langle \tilde{R}_1 \rangle$ , and then apply a second-order noise bias correction to obtain  $\langle R_1 \rangle$  (the expectation of the second term on the right-hand side of equation (25)):

$$\langle R_1 \rangle = \langle \tilde{R}_1 \rangle - \frac{1}{2} \left\langle \frac{\partial^2 R(\nu)}{\partial \nu_i \partial \nu_j} \right\rangle \langle \delta\nu_i \delta\nu_j \rangle_n + \mathcal{O}(\delta\nu^3). \quad (29)$$

The shear estimator is

$$\hat{\gamma}_1 = \frac{\langle e_1 \rangle}{\langle R_1 \rangle} + \mathcal{O}(\gamma^3) + \mathcal{O}(\delta\nu^3). \quad (30)$$

We observe that this method necessitates the calculation of second- and higher- order derivatives of the step function. The function's sharpness is modulated by the smoothness parameter; a larger parameter results in a gentler transition.

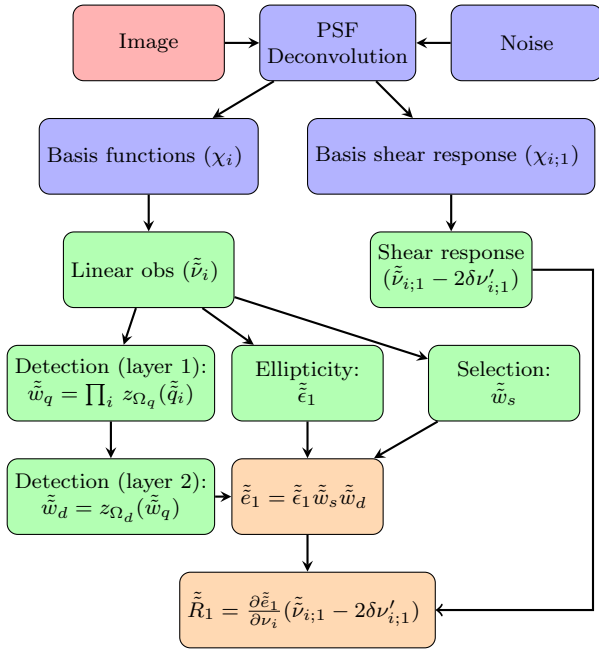


**Figure 2.** The workflow of AnaCal-FPFS from the input image to the output ellipticity and its shear response. To simplify the workflow, we only demonstrate the estimator for the first component of the shear. The workflow of our pipeline is summarized in Appendix A.

However, a caveat is that smaller smoothness parameters, which create a sharper selection function, lead to significant fluctuations in these higher order derivatives (see the lower panel of Figure 1). As a result, we are constrained to employing only smoothly transitioned cuts for our source detection and galaxy selection, which may lead to “ambiguous” detections near the peak of galaxy sources (Li & Mandelbaum 2023).

### 2.2.2 Renoising Approach

The technique of incorporating noise into images to develop a shear estimator free from noise bias, as outlined in this subsection, was first introduced by Sheldon & Huff (2017). The advantage of this method is that it does not require second- and higher-order derivatives of the nonlinear observables for noise bias correction. Furthermore, there is no need to approximate by ignoring the bias from higher-order noise. However, Sheldon & Huff (2017) did not provide a formal proof for the algorithm, and how it differs from the perturbation approach undertaken in Li & Mandelbaum (2023). In this study, we present an analytical formalism for correcting noise bias using renoised data, which builds on the foundational framework established by Li & Mandelbaum (2023). This advancement allows us to enhance our understanding of the noise bias correction technique proposed by Sheldon & Huff (2017), resulting in a significant increase in processing speed compared to the original numerical approach documented in Sheldon & Huff (2017).

Following Sheldon & Huff (2017), we add an additional layer of noise to the image, which possesses identical statistical properties after being rotated counterclockwise by  $90^\circ$ , where the rotation is specified within the space before PSF

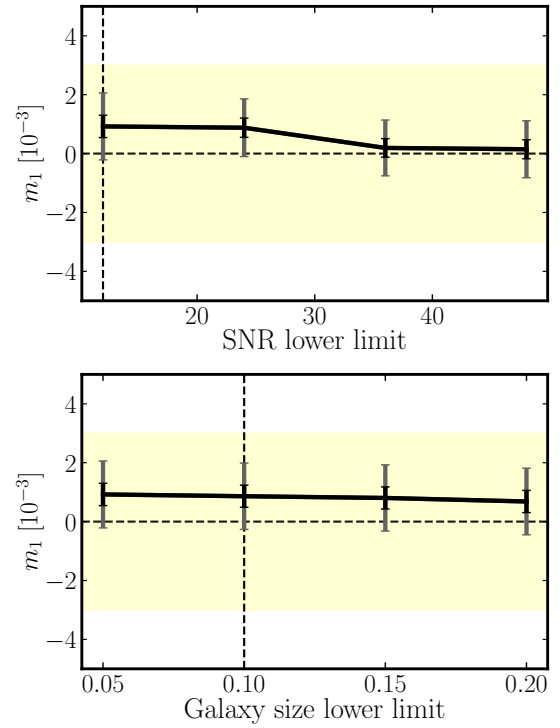


**Figure 3.** Multiplicative bias with  $1\sigma$  and  $3\sigma$  errors as a function of SNR lower limit (upper panel) and resolution lower limit (lower panel). The shaded region shows the LSST ten-year requirement on the control of multiplicative bias (The LSST Dark Energy Science Collaboration et al. 2018). The vertical lines are the default selection cuts on SNR ( $\text{SNR} > 12$ ) and galaxy size ( $R_2 > 0.1$ ).

smearing. The resulting additional measurement error on the linear observables are denoted as  $\delta\nu'$ , and they are characterized by a PDF denoted as  $P_n^{90}(\delta\nu')$ . This  $90^\circ$  rotation is applied to eliminate any spin-2 anisotropies present in the original noise image after deconvolution, which may stem from either the anisotropy in the noise correlation function or the PSF anisotropy leakage in the process of PSF deconvolution. Consequently, the ellipticity observed post-application of the additional noise image is:

$$\langle \tilde{e}_1 \rangle = \int_{\bar{\nu}, \delta\nu, \delta\nu'} \bar{P}_g(\bar{\nu}) e_1(T(\bar{\nu}) + \delta\nu + \delta\nu') \times P_n(\delta\nu) P_n^{90}(\delta\nu'). \quad (31)$$

To simplify the analysis, we define a new nonlinear observable:

$$G_1(T(\bar{\nu})) = \int_{\delta\nu, \delta\nu'} e_1(T(\bar{\nu}) + \delta\nu + \delta\nu') \times P_n(\delta\nu) P_n^{90}(\delta\nu'), \quad (32)$$

and equation (31) can be rewritten as

$$\langle \tilde{e}_1 \rangle = \int_{\nu} \bar{P}_g(\bar{\nu}) G_1(T(\bar{\nu})). \quad (33)$$

Again, before presenting the shear response of the renoised ellipticity  $\tilde{e}_{1,2}$ , we conduct a spin analysis to justify that the

first-order approximation is accurate to the second order of shear. As we assume that the noise is homogeneous, its statistical properties remain the same under a  $180^\circ$  rotation with respect to any reference point. Consequently,  $P_n P_n^{90}$  is invariant under a  $90^\circ$  rotation since the statistical property of the doubled noise remain unchanged under a  $90^\circ$  rotation. Additionally, given that  $e_1$  negates under a  $90^\circ$  rotation (see Section 2.1), it follows that  $G_1(\nu)$  also negates under a  $90^\circ$  rotation. Therefore,  $G_1(\nu)$  lacks both spin-0 and spin-4 components, necessitating solely the computation of its linear shear response to achieve a shear estimator accurate up to the second order of shear (see equations (16) and (17)).

To derive the shear response of the renoised ellipticity, we first determine the shear response of  $G_1(T(\tilde{\nu}))$  (adopting Einstein notation):

$$\left. \frac{\partial G_1(T(\tilde{\nu}))}{\partial \gamma_1} \right|_{\gamma=0} = \int_{\delta\nu, \delta\nu'} \frac{\partial e_1(\tilde{\nu})}{\partial \tilde{\nu}_i} \frac{\partial \tilde{\nu}_i}{\partial \gamma_1} \times P_n(\delta\nu) P_n^{90}(\delta\nu') \Big|_{\gamma=0}, \quad (34)$$

where  $\tilde{\nu}$  is the linear observable measured from the renoised image —  $\tilde{\nu} = T(\tilde{\nu}) + \delta\nu + \delta\nu'$ . Since image noise is not affected by lensing shear, the shear responses of  $\delta\nu$  and  $\delta\nu'$  are zero. Consequently, we have:

$$\partial \tilde{\nu}_i / \partial \gamma_1 = \partial \nu_i / \partial \gamma_1 = \nu_{;1i}. \quad (35)$$

However,  $\nu_{;1i}$  cannot be directly obtained in real observations due to the presence of noise in the images. The observed, renoised observable is:

$$\tilde{\nu}_{;1i} = \int_{\mathbf{k}} \tilde{f}(\mathbf{k}) \frac{\chi_{;1i}(\mathbf{k})}{p(\mathbf{k})}, \quad (36)$$

where  $\tilde{f}(\mathbf{k})$  is the renoised image in Fourier space. Similarly, we have the corresponding quantity defined for the image noise:

$$\delta\nu_{;1i} = \int_{\mathbf{k}} n(\mathbf{k}) \frac{\chi_{;1i}(\mathbf{k})}{p(\mathbf{k})}. \quad (37)$$

Thus, we can derive:

$$\frac{\partial \tilde{\nu}_i}{\partial \gamma_1} = \nu_{;1i} = \tilde{\nu}_{;1i} - \delta\nu_{;1i} - \delta\nu'_{;1i}, \quad (38)$$

and the shear response of the expectation of the renoised ellipticity is

$$\left\langle \frac{\tilde{R}_1}{\tilde{\nu}_i} \right\rangle = \left\langle \frac{\partial e_1(\tilde{\nu})}{\partial \tilde{\nu}_i} \left( \tilde{\nu}_{;1i} - \delta\nu_{;1i} - \delta\nu'_{;1i} \right) \Big|_{\gamma=0} \right\rangle. \quad (39)$$

Note that  $\delta\nu'$  can be measured because the noise is generated through simulation and we know the exact noise realization; in contrast,  $\delta\nu$ , which represents the noise in actual images, cannot be directly measured since reconstructing the exact noise realization from the image is unfeasible. However, given that  $\delta\nu'$  and  $\delta\nu$  are from noise realizations oriented  $90^\circ$  relative to each other in the pre-PSF plane, and considering the random orientation of galaxies, it follows that:

$$\left\langle \frac{\partial e_1(\tilde{\nu})}{\partial \tilde{\nu}_i} \Big|_{\gamma=0} \delta\nu'_{;1i} \right\rangle = \left\langle \frac{\partial e_1(\tilde{\nu})}{\partial \tilde{\nu}_i} \Big|_{\gamma=0} \delta\nu_{;1i} \right\rangle. \quad (40)$$

We refer readers to Appendix B for the proof. Therefore, the

expectation of the shear response of the renoised ellipticity can be measured with the simulated noise:

$$\left\langle \frac{\tilde{R}_1}{\tilde{\nu}_i} \right\rangle = \left\langle \frac{\partial e_1(\tilde{\nu})}{\partial \tilde{\nu}_i} \left( \tilde{\nu}_{;1i} - 2\delta\nu'_{;1i} \right) \right\rangle, \quad (41)$$

and the shear estimator is

$$\hat{\gamma}_1 = \frac{\langle \tilde{e}_1 \rangle}{\left\langle \frac{\tilde{R}_1}{\tilde{\nu}_i} \right\rangle} + \mathcal{O}(\gamma^3). \quad (42)$$

In summary, by introducing the additional noise, we eliminate the spin-2 anisotropy from the original image noise on the image plane prior to PSF convolution. Furthermore, we utilize this added noise, whose realization are exactly known, to estimate the shear response of the renoised image. It is worth noting that, the “renoising” approach eliminates the need for any truncation in the perturbative series for the noise bias correction. Consequently, equation (42) does not include the high-order terms from image noise,  $\mathcal{O}(\delta\nu^3)$ , which are present in equation (30).

Both the perturbation and “renoising” approaches involve trade-offs between variance and bias. For the perturbation method, the second-order noise bias correction term for ellipticity, measured from a noisy image, increases the statistical uncertainty in the shear estimation. Similarly, in the “renoising” approach, the additional noise doubles the variance of the image noise, also increasing the variance in shear estimation. As a result, the effective galaxy number density is reduced by 20% to 25% compared to using a biased shear estimator without noise bias correction.

The workflow of the algorithm from input image to the output shape and the corresponding shear response is demonstrated in Figure 2 and outlined in Appendix A. We note that this noise bias correction does not involve second- or higher-order derivatives during the detection process. This allows us to apply a second layer of detection using step functions with small smoothness parameters to avoid “ambiguous” detection (see the layer 2 in Figure 2). To be more specific, in the first detection layer, we measure the preliminary detection weight:  $\tilde{w}_q$  using the value difference between neighboring pixels to select peak candidates following Li et al. (2024). The second layer applies another step function on  $\tilde{w}_p$  to derive the final detection weight:  $\tilde{w}_d = z_{\Omega_d}(\tilde{w}_q)$ , where  $z_{\Omega_d}$  is the step function with a small smoothness parameter  $\Omega_d = 0.04$ . We find that, due to this improved detection, the effective galaxy number density is improved by approximately 15% compared to the earlier version of the code adopting the second-order noise bias correction in Li et al. (2024). More specifically, we have observed that the second-order noise bias correction term for ellipticity in equation (26) becomes particularly noisy when either the selection weight or the detection weight has a large gradient. As illustrated in Figure 1, the noise bias correction terms that incorporate second-order derivatives display significant fluctuations under conditions of selection weight function with a small smoothness parameter. This instability leads to considerable uncertainty in shear estimation in noisy images. Moreover, employing a detection weight function with a large smoothness parameter results in numerous sub-peaks near the galaxy center where the weight is nonzero, which cannot be applied to real observations. Additionally, it is worth noting that the “renoising” approach does not require any noisy second-order derivatives so that

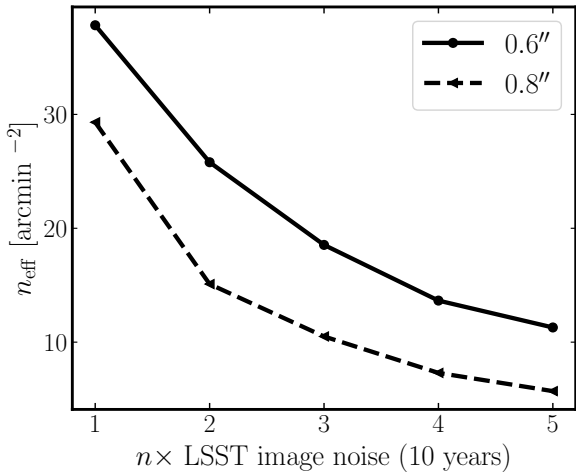


**Figure 4.** This figure illustrates the effective galaxy number density, normalized so that the effective standard deviation of shape noise per component is 0.26. The data combines information from four bands: “griz”. The calculation of the effective galaxy number density is based on the anticipated noise level of the ten-year LSST coadds. The solid line (dashed) is for the PSF seeing 0.6” (0.8”). Actual observations may yield different values.

we are able to adopt multiple detection layers with small smoothness parameters. Moreover, it avoids the need for any truncation in the perturbative series for the noise bias correction. Therefore, we adopt the “renoising” approach as the default noise bias correction method in **AnaCal**.

However, a limitation of this noise bias correction method is that we need to double the image noise before detection and measurement. It worth noting that a recent paper (Zhang et al. 2023) suggests using deep field images from the same survey to mitigate the image noise in such correction strategies. We intend to apply the methodology of Zhang et al. (2023) in our analytical shear estimation framework in future work.

### 3 TEST ON IMAGE SIMULATIONS

In this section, we evaluate our shear estimation algorithm using LSST-like image simulations under various conditions, as detailed in Section 3.1. The results for different galaxy sample selections are presented in Section 3.2. Section 3.3 examines the effects of different PSF anisotropies, while Section 3.4 discusses the impact of varying levels of PSF variation across the coadded image cells. The influence of anisotropy in the noise correlation function is detailed in Section 3.5. Section 3.6 addresses the results under various levels of stellar contamination. Finally, Section 3.7 evaluates the algorithm’s performance in the presence of bright stars and pixel artifacts.

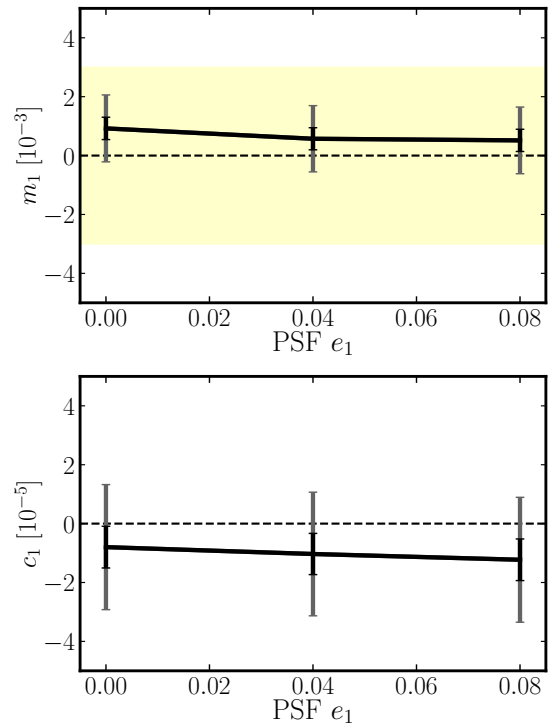


**Figure 5.** Multiplicative bias (upper panel) and additive bias (lower panel) with  $1\sigma$  and  $3\sigma$  errors as a function of PSF anisotropy. The shaded region are the LSST ten-year requirement on the control of systematic bias (The LSST Dark Energy Science Collaboration et al. 2018).

#### 3.1 Simulation

We employ the package `descwl-shear-sims`<sup>2</sup> as presented in Sheldon et al. (2023) for image simulations. This package renders images using the `GalSim` package (Rowe et al. 2015). The simulation package generates calibrated images with subtracted background and provides an estimated noise variance image plane. Additionally, it includes a world coordinate system (WCS) transformation and a position-dependent point spread function (PSF) model. Areas of concern such as saturation, star bleeds, cosmic rays, and defective columns are identified and flagged within an integer bit mask image plane for easy reference. We do not simulate scenarios involving miscalibrated input data. Specifically, we omit testing the effects of inaccuracies in PSF models, noise estimates, image warping, image coadding, astrometric or photometric calibrations. Our primary aim is to evaluate the effectiveness of our shear estimator using coadd images whose characteristics are well understood. However, to fully assess the final shear calibration in real data analyses, it might become essential to either propagate or simulate the impact of miscalibrated data. We note that all of the simulations that are used to test our shear estimation includes galaxy blending. Additionally the simulations adopt a constant shear, where

<sup>2</sup> <https://github.com/LSSTDESC/descwl-shear-sims>



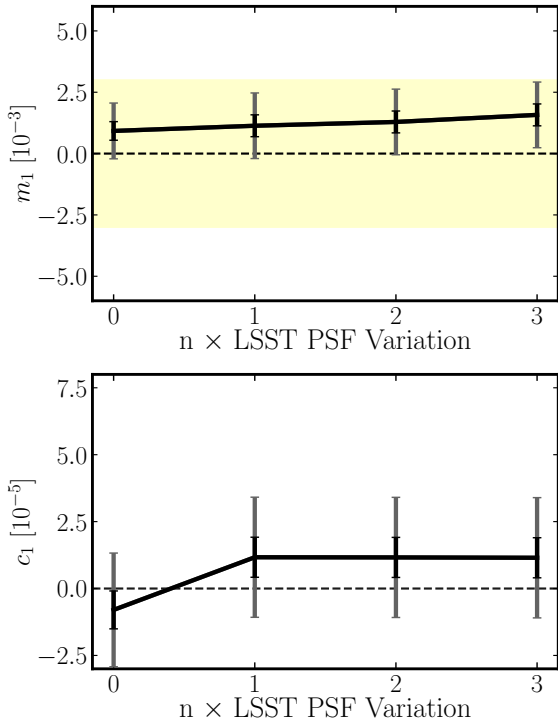


**Figure 6.** Multiplicative bias (upper panel) and additive bias (lower panel) as a function of PSF variation, with  $1\sigma$  and  $3\sigma$  errors. The shaded region shows the LSST ten-year requirement on the control of multiplicative bias (The LSST Dark Energy Science Collaboration et al. 2018).

all blended galaxies within a single image experience identical shear distortions. Both the galaxy shapes and the positions are changed by the shear. The shear applied in these simulations is  $\gamma_1 = \pm 0.02$ . The simulation is divided into 10000 subfields for each test case, and each subfield is 0.06 square degrees. We adopt the ring test (Massey et al. 2007) by creating a  $90^\circ$  rotated companion for each subfield. Additionally, we use the shape noise cancellation proposed by Pujol et al. (2019) to reduce uncertainty on the estimated shear caused by intrinsic shape dispersion and image noise.

Our basic image simulation adopts an LSST-like PSF, for which the PSF image is modelled with a Moffat (1969) profile:

$$p_m(\mathbf{x}) = \left[ 1 + c \left( \frac{|\mathbf{x}|}{r_P} \right)^2 \right]^{-2.5}, \quad (43)$$

where  $r_P$  and  $c$  are set such that the full width at half maximum (FWHM) of the Moffat PSF is  $0''.80$ , matching the expected median seeing of LSST images. Note that we start with a circular PSF and examine asymmetric PSFs later in Section 3.3.

Due to the high sky background, we simulate the residual Poisson noise in each image by applying Gaussian noise after the background subtraction. We utilized the

WeakLensingDeblending<sup>3</sup> package (Sanchez et al. 2021) to estimate the image noise tailored to the LSST filter specifications. After rendering all image features and introducing noise, we standardized the images to a consistent zero point of 30.

In this paper, we simulate coadded images in the “griz” bands using the anticipated ten-year LSST noise levels as our standard simulation setup, unless otherwise noted. The input galaxy models are generated using the WeakLensingDeblending package. These models feature galaxies with bulge, disk, and AGN components, all sharing the same morphology across different bands. The bulge and disk components can have different fluxes and ellipticities, and the AGN is modeled as point source at galaxy center. The catalog boasts a raw density of 240 galaxies per square arcminute and has an effective i-band AB magnitude limit of 27. Galaxies are randomly distributed in the image without taking into account clustering of galaxy positions.

We quantify the bias in the shear estimation using multiplicative ( $m_{1,2}$ ) and additive ( $c_{1,2}$ ) biases (Huterer et al. 2006; Heymans et al. 2006). Specifically, the estimated shear,  $\hat{g}_{1,2}$ , is related to the true shear,  $g_{1,2}$ , as

$$\hat{g}_{1,2} = (1 + m_{1,2}) g_{1,2} + c_{1,2}. \quad (44)$$

We adopt 90 degree rotation (Massey et al. 2007) and the technique introduced in Pujol et al. (2019) to reduce shape noise in the estimation of multiplicative and additive biases.

### 3.2 Galaxy Properties

In this subsection, we demonstrate the performance of our shear estimator using simple image simulations characterized by isotropic PSFs and uniform noise levels. The PSF remains constant across the image, and we avoid complications from image artifacts such as bad CCD columns or cosmic rays. Moreover, these simulations only include galaxies and omit stars. We focus on testing the performance of the shear estimator with different selection cuts on galaxy SNR and size.

In Figure 3, we present the multiplicative bias as a function of the lower limit of galaxy SNR in the upper panel, and as a function of the lower limit of galaxy size in the lower panel. We find that the multiplicative biases for these cuts are all below the LSST science requirement on the control of multiplicative shear bias (The LSST Dark Energy Science Collaboration et al. 2018). Since no significant additive bias is detected in this analysis, it is not included in the plots. We refer readers to Li & Mandelbaum (2023) for the definition of galaxy size ( $R_2$ ) and SNR. In the remainder of this paper, unless otherwise specified, we adopt  $\text{SNR} > 12$ ,  $R_2 > 0.1$  as the default criteria for galaxy selection.

Additionally, we have estimated the effective galaxy number density for varying noise levels. Our definition of effective galaxy number density is normalized such that the effective standard deviation of shape noise per component is 0.26. Our estimation strictly adheres to equation (5) from Li et al. (2024). Specifically, we simulate numerous exposures with blended galaxies (with different galaxy populations, orientations and image noises) and obtain the shear estimation uncertainty using all detections within one square arcminute.

<sup>3</sup> <https://github.com/LSSTDESC/WeakLensingDeblending>

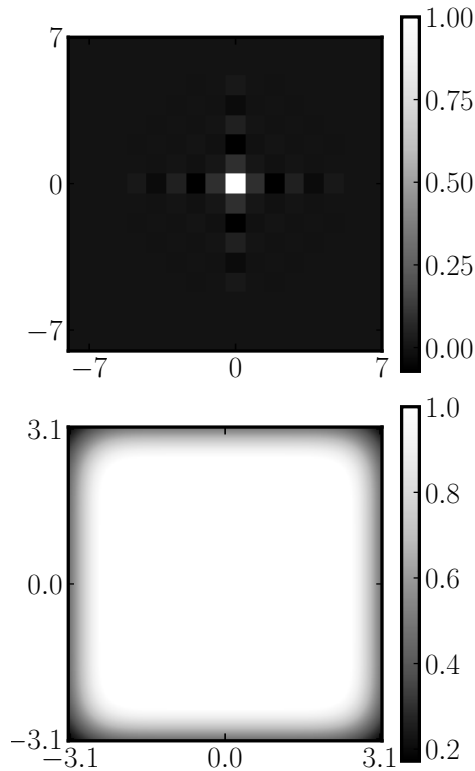


**Figure 7.** The two-point statistics of homogeneous Gaussian noise. The upper panel shows the noise correlation function in configuration space, and the lower panel shows the power spectrum in Fourier space within the Nyquist wavenumber. These two-point statistics are normalized such that the maximum is 1. For illustration purposes in the figure, the pixel scale is set to 1, resulting in a Nyquist wavenumber of  $\pi$ .

The uncertainty in shear estimation is denoted as  $\sigma_g$ . We then calculate the number of galaxies with an intrinsic shape noise of 0.26 required to achieve this level of uncertainty, determining the estimated effective galaxy density per square arcminute. The effective galaxy number density is

$$n_{\text{eff}} = \left( \frac{0.26}{\sigma_g} \right)^2 [\text{arcmin}^{-2}]. \quad (45)$$

Compared to other methods of measuring effective galaxy number density by counting galaxies with specific weights (Chang et al. 2013), our approach accounts for the correlation between shape measurements of neighboring detections. This correlation arises because a single image pixel can contribute to the measurements of multiple neighboring galaxies when they are blended. The corresponding results are presented in Figure 4. This analysis utilizes data from the four-band “*griz*” combination, and the “*reinoising*” approach is adopted for noise bias correction. In the simulations, the galaxy morphology and the PSF model are exactly the same across all bands. Similar to Li et al. (2024), we combine images from different bands by adding them with inverse-variance weights. It is important to note that the effective galaxy number density is estimated based on the expected noise levels from ten years of LSST coadds and the anticipated median PSF size. However, the absolute value of the effective number density

may not be realistic since we have not precisely calibrated the number density in the simulations to any real dataset.

### 3.3 Anisotropy from PSF

In this subsection, we show the performance of our shear estimator on image simulations with different values for the PSF anisotropy. To simulate these images, the Moffat PSF model defined in equation (43) is sheared to exhibit an ellipticity of  $(e_1 = e_{\text{psf}}, e_2 = -e_{\text{psf}})$ , where  $e_{\text{psf}}$  represents the PSF anisotropy, varying between 0 and 0.08. For the PSFs with small ellipticities, the relation between ellipticity and shear is approximately:  $e_{1,2} \sim 2g_{1,2}$ .

The results depicted in Figure 5 demonstrate that changes in PSF anisotropy do not significantly impact either the multiplicative or additive shear biases. The multiplicative bias remains below the LSST requirement, and the additive bias is statistically consistent with zero. Notably, even in the most extreme scenario with  $e_{\text{psf}} = 0.08$ , the magnitude of the additive bias remains below  $3 \times 10^{-5}$ . We also calculate the fractional additive bias, defined as the ratio of the additive bias to the PSF ellipticity (Mandelbaum et al. 2018a; Li et al. 2022a):

$$a_{1,2} \equiv \frac{c_{1,2}}{e_{1,2}^{\text{PSF}}}, \quad (46)$$

and we report a fractional additive bias of  $a_1 = (1.6 \pm 1.1) \times 10^{-4}$ , which is consistent with zero.

### 3.4 PSF Variation

We create spatially variable PSF models by modifying the basic Moffat PSF model (equation (43)), varying both the ellipticity and size of the PSFs across the image. The simulation methods are detailed in Appendix A of Sheldon et al. (2020) and build upon the approach proposed by Heymans et al. (2012). Heymans et al. (2012) utilized images with high stellar density to fit a von Kármán model of atmospheric turbulence (von Kármán 1948) to account for PSF variations. Meanwhile, Sheldon et al. (2020) refined this algorithm by reducing unrealistically high power below one arcsecond, thus generating realizations of spatially variable PSFs using Gaussian random fields. In the image simulation, we model the PSF ellipticity and size at different positions as a Gaussian random field, using correlation functions from Heymans et al. (2012). To account for variations, we use a PSF variation parameter that modulates the variance of the Gaussian random field to simulate PSF field with different levels of variation.

In our detection and shape measurement process, we employ a constant point spread function (PSF) across each coadded image cell (Armstrong et al. 2024), which measures 250 by 250 pixels. This constant PSF is sampled at the center of the image cell. Specifically, our shear inference approach does not capture spatial variations of the PSF below scales of  $\sim 250$  pixels. Each neighboring cell includes an overlapping region of 50 pixels. Figure 6 illustrates the performance of the shear estimator for different levels of PSF variation. In Figure 6, we normalize the variation of the PSF by the expected PSF variance for cell-based coadds in the final year of the Rubin LSST survey (Sheldon et al. 2020). We observe that the multiplicative bias increases slightly with greater PSF variation,

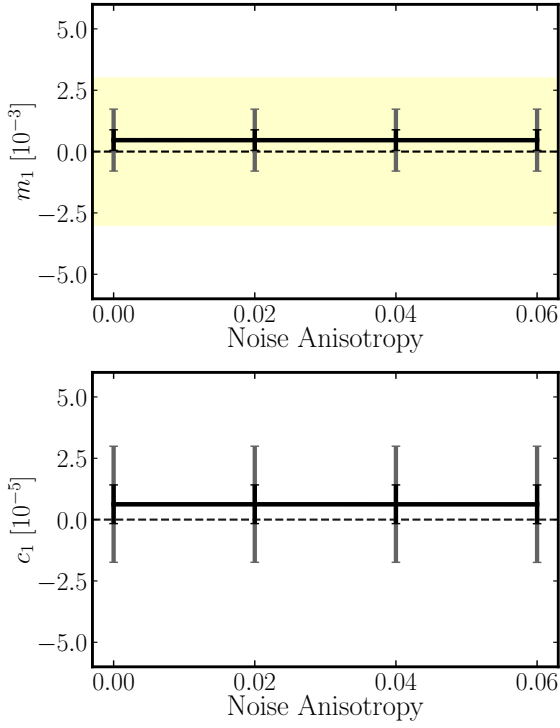


**Figure 8.** Multiplicative bias (upper panel) and additive bias (lower panel) with  $1\sigma$  and  $3\sigma$  errors as a function of noise anisotropy (quantified by the shear distortion on noise correlation function). The shaded region shows the LSST ten-year requirement on the control of multiplicative bias (The LSST Dark Energy Science Collaboration et al. 2018).

whereas the additive bias remains consistently zero. It is important to note that the multiplicative bias arises from using a constant PSF sampled at the center of each cell. Even at a variance three times that expected in the LSST, the multiplicative bias remains within acceptable LSST standards. The results for estimation of the second component of the shear is consistent with the first component of shear demonstrated in Figure 3.

### 3.5 Anisotropic Noise

In this subsection, we evaluate our algorithm’s performance in the presence of noise with various anisotropic correlations due to the image warping. Operating under the assumption that the noise correlation function can be precisely measured in real observations, our aim is to determine whether we can mitigate the bias introduced by correlated noise, provided that we have an accurate assessment of its correlation function. Testing the performances of image warping and coadding are beyond the scope of this paper.

We focus on anisotropic (square-like) correlations between adjacent pixels, which match the autocorrelation function of a third-order ( $a = 3$ ) Lanczos kernel, which was used to warp and coadd images taken during the first-year HSC survey

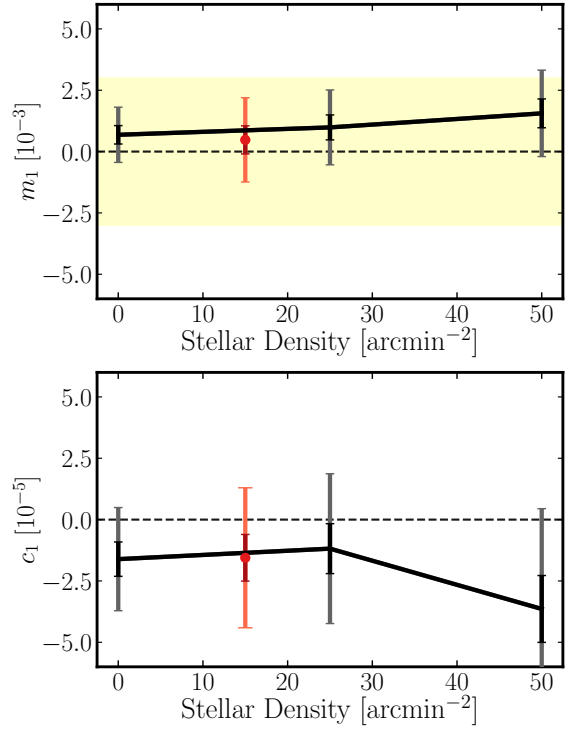


**Figure 9.** Multiplicative bias (upper panel) and additive bias (lower panel) with  $1\sigma$  and  $3\sigma$  errors as a function of stellar density in the simulation. The “•” points indicate the biases, as established through simulations where the stellar density for each subfield is randomly drawn from the DC2 simulation across the LSST survey. The shaded region shows the LSST ten-year requirement on the control of multiplicative bias (The LSST Dark Energy Science Collaboration et al. 2018).

(Bosch et al. 2018):

$$L(\mathbf{x}) = \begin{cases} \text{sinc}\left(\frac{x}{a}\right) \text{sinc}(x) \text{sinc}\left(\frac{y}{a}\right) \text{sinc}(y) & |x|, |y| < a \\ 0 & \text{otherwise,} \end{cases} \quad (47)$$

where  $\text{sinc}(x) = \sin(\pi x)/\pi x$ ;  $x$ ,  $y$  and  $a$  are in pixel units. Since the third-order Lanczos kernel is undersampled for the pixel size in the observation, we estimate the correlation function using a finer pixel scale where the Lanczos kernel is oversampled, which is equivalent to estimating the correlation function from the coadded noise images from single exposure with random subpixel offsets after warping with the Lanczos kernel. The correlation function and power spectrum below the Nyquist wavenumber are shown in Figure 7. The noise correlation function exhibits a pattern similar to the average noise correlation function derived from the blank pixels in the HSC coadded images, as illustrated in Figure 1 of Mandelbaum et al. (2018b). This correlation function shows a stronger variation along the  $x$  and  $y$  axes, which can be attributed to the properties of the Lanczos kernel. Unlike some observations (e.g., HSC and LSST), where single exposures undergo different rotations, no rotation is applied when generating the effective noise correlation function. The power spectrum is computed using a Discrete Fourier Transform of the correlation function. To prevent the influence of periodic

boundary conditions in the computation of Discrete Fourier Transform, the stamp size for the Fourier transform is set significantly larger than the size of the Lanczos kernel. In addition, the Fourier transform is performed on the finer pixels to reduce the aliasing effect on the power spectrum due to the undersampling. In the simulation, we generate a normalized white noise field and filter it according to the noise power spectrum below the Nyquist wavenumber. We then rescale the noise field to match a target noise variance. The noise applied in this test is homogeneous and Gaussian since (a) inhomogeneous noise originating from galaxy sources plays a minor role and (b) the high sky background level in ground-based observations, such as Rubin LSST, means the Poisson noise from the background is effectively Gaussian.

To simulate various noise anisotropy levels, we distort the noise correlation function using a shear ranging from 0 to 0.06 to stretch the noise correlation function in the horizontal direction. In the image processing, we assume that we know the exact noise correlation function after the distortion. In Figure 8, we depict both multiplicative and additive biases as functions of the shear distortion applied to the noise correlation function. As demonstrated, the biases in the shear estimator remain consistently consistent with zero.

### 3.6 Stellar Contamination

This subsection assesses the impact of stellar contamination on shear estimation. As demonstrated in Li et al. (2022b), when sources are isolated, both the ellipticity and shear response expectation values for a star sample are zero. Thus, while stellar contamination does introduce variance to the estimates, it does not bias them in cases involving isolated sources. However, this observation cannot be extended to situations where sources are blended. In blended scenarios, the position of stars—predominantly from the Milky Way—is unaffected by lensing distortions. Consequently, when stars and galaxies are blended, it leads to contamination of the shear signal in distant galaxies.

To evaluate the accuracy of shear estimation in scenarios characterized by blending with stellar density distributions, we performed simulations using blended images. These simulations incorporated stars with fluxes and densities akin to those found in the Milky Way, as derived from the LSST DESC Data Challenge Two (DC2) simulation catalogs, as reported by LSST Dark Energy Science Collaboration (LSST DESC) et al. (2021). In each simulated field, stars are randomly sampled with replacement from the stellar density map utilized in the DC2 simulation, with densities exceeding 100 per square arcminute being excluded. For this test, we omitted stars brighter than magnitude 18 in  $r$ -band, while in the subsequent section, we will specifically examine the impact of the bright-star mask on shear estimation. It is important to note that the specified stellar density refers to the total number of stars input into the simulation, not those actually detected. Each star is modeled as a point source convolved with a PSF.

Results from this test are indicated by “•” points in Figure 9, showing that both multiplicative and additive shear biases are consistently close to zero. The average stellar density for these samples is approximately  $18 \text{ arcmin}^{-2}$ . Further detailed tests are conducted with fixed input stellar densities ranging from 0 to  $50 \text{ arcmin}^{-2}$ . These results, also shown in

Figure 9, indicate that even at an extremely high stellar density ( $50 \text{ arcmin}^{-2}$ ), neither the multiplicative nor the additive biases are significant (i.e., less than  $3\sigma$ ). Moreover, the multiplicative shear bias remains below the LSST’s requirements, even in this extreme case.

### 3.7 Bright Star and Pixel Masks

In this subsection, we evaluate the performance of the shear estimator in simulations that include bright stars and image artifacts such as saturation, bleeds, bad CCD columns, and cosmic rays. The simulation follows Sheldon et al. (2023).

We continue to randomly sample stars from the stellar density map used in the DC2 simulation. Unlike Section 3.6, which only includes stars fainter than magnitude 18, this simulation includes all stars, even those that are brighter. To mimic saturation, we limited the value in each pixel, flagged saturated pixels in the integer bitmask image of the exposure, and set the variance for these pixels to infinity. Although we did not simulate nonlinear detector responses, we overlaid saturated stars with bleed trail images from pre-generated templates that match the star’s flux in the relevant filter. We flag these pixels with bleed trails appropriately in the bitmask.

For cosmic rays, we randomly determined their location, angle, and length (between 10 and 30 pixels) on the image. We flagged the affected pixels and ensured adjacent pixels were also flagged if they touched corners. These pixels were set to NaN in the image data, and a cosmic ray bit is added to the bitmask for later interpolation, preventing their use in the final shear estimates.

Additionally, we used a modified Monte Carlo generator from Becker et. al (in prep.) to simulate bad columns. Each column, just a pixel wide and randomly positioned, included random gaps to reflect columns that do not extend across the entire CCD. Each image included at least one such bad column. The bad columns are flagged in the bitmask.

Our masking algorithm is divided into two steps. In the first step, we apply circular binary masks to stars with a magnitude brighter than 18, extending out to the radius where the star’s profile met the  $1\sigma$  noise level of the image. It is important to note that in real-world scenarios, such masks would be algorithmically determined. These masked regions near bright stars are set to zero. Pixels affected by image artifacts, including star bleeds, cosmic rays, and bad columns, are also zeroed out. The left panel of Figure 10 shows a masked image before detection and measurement, and the right panel shows the mask plane.

In the second step, we aim to identify sources in close proximity to the edge of the mask that have been significantly impacted by the masking process setting the pixels in the masked region to zero. Specifically, we make a continuous smoothed version of this binary mask in the first step and record the mask value from the smoothed mask at the position of the detected peak. A higher mask value indicates closer distance to the masked region and greater influence of the masking on the source. Then we eliminate detections at pixels falling above a threshold in this smoothed mask. The smoothing kernel is a 2D Gaussian, with a standard deviation matching the scale of the shapelet kernel used in the FPFS shear estimator (Li et al. 2018). The Gaussian kernel is truncated at three times its standard deviation. The Gaussian

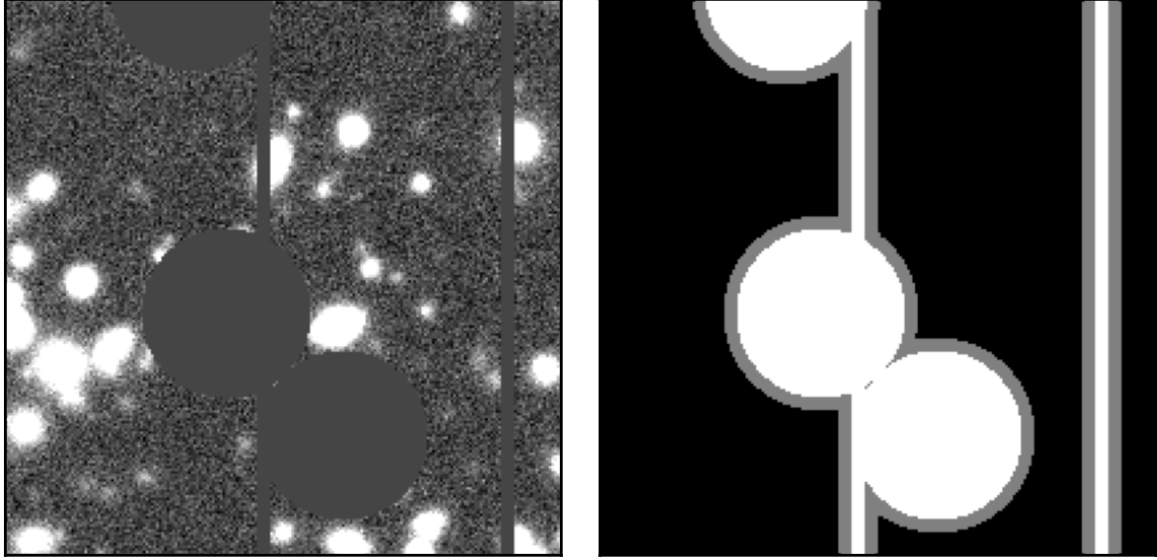


**Figure 10.** The left panel displays the image plane with a mask applied prior to the detection and measurement process. The right panel illustrates the mask plane itself. In the right panel, the white pixels represent regions that were masked before detection and measurement. The grey pixels indicate areas within the extended mask where sources have a mask value exceeding 20 (see vertical lines in Figure 11). These sources are subsequently excluded from the catalog.

kernel is normalized to a flux of 1000, and we retain only the integer part of the mask value to save storage space. Essentially, we increase the mask region and remove the detection in the extended masked region. We note that the mask value is not dependent on lensing shear distortion; therefore, this selection does not cause selection bias.

In Figure 11, we illustrate the accuracy of the shear estimator across different upper limits on the mask value. We find that when increasing the upper limit to allow more sources near the masked regions, the amplitude of multiplicative bias slightly increases where the amplitude of additive bias significantly increases. We find a significant negative additive bias on the first component of shear if we do not remove galaxies close to the mask using the mask value due to the vertical orientation of all bad columns and bleed features in our simulation. This is because random camera rotation is not applied in the simulation. However, in the real LSST observations, single visits at a particular spot have random orientations. The average additive bias on sources that are close to the masked region should be smaller than what we found here. Therefore, our selection and masking strategy is conservative for the real LSST observations. Based on these findings, we recommend setting the upper limit on the mask value to 20. As depicted in Figure 11, this threshold ensures the multiplicative bias meets LSST standards and the additive bias remains consistent with zero within the statistical uncertainty of the test. Additionally, we report that the additive systematic bias related to masking is below  $4 \times 10^{-5}$ , although the LSST DESC’s requirement on the control of additive bias has not been decided. The increased masked region for this threshold is demonstrated as a grey region in the right panel of Figure 10.

#### 4 SUMMARY AND OUTLOOK

This paper provides a comprehensive review and analytical proof of the noise bias correction method for weak lensing shear inference, specifically focusing on the “renoising” technique utilized within the METACALIBRATION framework. We have integrated this analytical approach into the AnaCal shear estimation framework and introduced several significant enhancements to improve the robustness and accuracy of the noise bias correction algorithm. To validate our modified algorithm, we conducted simulations meticulously designed to emulate the imaging characteristics of the LSST. These simulations included semi-realistic galaxies and stars, characterized by distributions of magnitudes and spatial densities that mirror those expected in actual observational data.

We rigorously tested our algorithm against a variety of challenging observational conditions typical in high-precision astronomy. This included images affected by cosmic rays, defective CCD columns, issues arising from bright star saturation, bright star “bleed trails”, and variations in the point spread functions (PSFs) across the coadded image cell. The rigorous testing regime was crafted to closely replicate the stringent conditions under which the LSST operates assuming perfectly calibrated data — perfect astrometry, PSF modeling and masking.

The outcomes of our tests are promising, indicating that the multiplicative shear bias in our algorithm is consistently less than 0.2 percent even under many extreme conditions. The performance of our algorithm meets the demanding requirement set by the LSST survey (The LSST Dark Energy Science Collaboration et al. 2018) even under many extreme conditions, ensuring that it is well-suited for high-stakes applications in cosmology where precision is paramount. This substantiates the efficacy of our enhancements and the potential of our approach to contribute significantly to the field

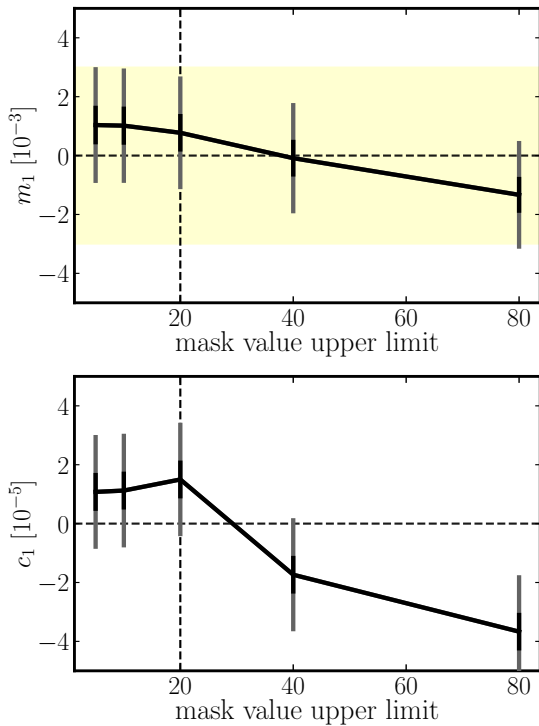


**Figure 11.** Multiplicative bias (upper panel) and additive bias (lower panel) with  $1\sigma$  and  $3\sigma$  errors as a function of the upper limit on the mask value. The vertical dashed line is the default upper limit on the mask value adopted in this paper to remove galaxies close to masked region. The shaded region are the LSST ten-year requirement on the control of systematic bias (The LSST Dark Energy Science Collaboration et al. 2018).

of precision astronomy. Our algorithm achieves exceptional computational speeds, processing each galaxy in less than a millisecond. It can process all coadded images from the Rubin LSST using just a few thousand CPU hours. The minimal computational resources required allow us to conduct a large number of systematic tests on real observations even with limited resources, ensuring that the shear measurements are sufficiently accurate for weak lensing science. For instance, if we detect any additive systematics during the null test that correlate with the observational conditions of the survey, this would enable us to adjust the image processing code. We could then rerun the entire sequence from the coadded image onward to mitigate the identified systematics.

The `METADETECTION` algorithm has been validated in Sheldon et al. (2023) and will be applied to the LSST data. Since different shear estimators take different assumptions, cross comparisons of any scientific results between the catalogs from different shear estimators on the observed data are valuable.

This paper primarily focuses on evaluating the algorithm using constant-shear simulations, in which all blended galaxies within a single image undergo identical shear distortions. For simulations that incorporate redshift-dependent shear, it may be necessary to simulate images that allow for the joint calibration of both the redshift-dependent shear and the redshift distribution of the source galaxies (MacCrann et al.

2022; Li et al. 2023) The implications of redshift-dependent shear will be explored in our future research.

## ACKNOWLEDGEMENTS

This paper has undergone internal review in the LSST Dark Energy Science Collaboration. The primary authors would like to thank the internal reviewers Arun Kannawadi and Gary Bernstein. We thank Erin Sheldon and Matthew Becker for the help on using the package `descwl-shear-sims` and the comments on the paper. In addition, we thank Erin Sheldon for comments on the paper draft.

This paper makes use of software developed for the Vera C. Rubin Observatory. We thank the Vera C. Rubin Observatory for making their code available as free software at <http://dm.lsst.org>.

We thank the maintainers of NumPy (Harris et al. 2020), SciPy (Virtanen et al. 2020), Matplotlib (Hunter 2007), GalSim (Rowe et al. 2015) and conda-forge (conda-forge community 2021) projects for their excellent open-source software and software distribution systems.

Xiangchong Li and Rachel Mandelbaum are supported by the Department of Energy grant DE-SC0010118. Xiangchong Li is an employee of Brookhaven Science Associates, LLC under Contract No. DE-SC0012704 with the U.S. Department of Energy.

The DESC acknowledges ongoing support from the Institut National de Physique Nucléaire et de Physique des Particules in France; the Science & Technology Facilities Council in the United Kingdom; and the Department of Energy, the National Science Foundation, and the LSST Corporation in the United States. DESC uses resources of the IN2P3 Computing Center (CC-IN2P3-Lyon / Villeurbanne - France) funded by the Centre National de la Recherche Scientifique; the National Energy Research Scientific Computing Center, a DOE Office of Science User Facility supported by the Office of Science of the U.S. Department of Energy under Contract No. DE-AC02-05CH11231; STFC DiRAC HPC Facilities, funded by UK BEIS National E-infrastructure capital grants; and the UK particle physics grid, supported by the GridPP Collaboration. This work was performed in part under DOE Contract DE-AC02-76SF00515.

Author contributions to this work are as follows: Xiangchong Li developed the mathematical theory for the noise bias correction theory and designed the pipeline for image simulation and shear estimation. Rachel Mandelbaum supervised the project, providing valuable discussions and feedback on the paper.

## DATA AVAILABILITY

The code used for this paper is publicly available on Github: <https://github.com/mr-superonion/AnaCal/tree/v0.1.6>

## REFERENCES

- Akeson R., et al., 2019, *arXiv e-prints*, p. [arXiv:1902.05569](https://arxiv.org/abs/1902.05569)
- Armstrong R., et al., 2024, *arXiv e-prints*, p. [arXiv:2407.01771](https://arxiv.org/abs/2407.01771)
- Bartelmann M., Schneider P., 2001, *Physics Reports*, 340, 291
- Bernstein G. M., Armstrong R., 2014, *MNRAS*, 438, 1880

Bernstein G. M., Jarvis M., 2002, *AJ*, 123, 583

Bernstein G. M., Armstrong R., Krawiec C., March M. C., 2016, *MNRAS*, 459, 4467

Bosch J., et al., 2018, *PASJ*, 70, S5

Bradbury J., et al., 2018

Chang C., et al., 2013, *MNRAS*, 434, 2121

Harris C. R., et al., 2020, *Nature*, 585, 357

Hazimeh H., Ponomareva N., Mol P., Tan Z., Mazumder R., 2020, in III H. D., Singh A., eds, Proceedings of Machine Learning Research Vol. 119, Proceedings of the 37th International Conference on Machine Learning. PMLR, pp 4138–4148, <https://proceedings.mlr.press/v119/hazimeh20a.html>

Heymans C., et al., 2006, *MNRAS*, 368, 1323

Heymans C., Rowe B., Hoekstra H., Miller L., Erben T., Kitching T., van Waerbeke L., 2012, *MNRAS*, 421, 381

Huff E., Mandelbaum R., 2017, preprint, (arXiv:1702.02600)

Hunter J. D., 2007, *Computing in Science and Engineering*, 9, 90

Huterer D., Takada M., Bernstein G., Jain B., 2006, *MNRAS*, 366, 101

Ivezić Ž., et al., 2019, *ApJ*, 873, 111

Kaiser N., 2000, *ApJ*, 537, 555

Kilbinger M., 2015, *Reports on Progress in Physics*, 78, 086901

LSST Dark Energy Science Collaboration (LSST DESC) et al., 2021, *ApJS*, 253, 31

Laureijs R., et al., 2011, preprint, (arXiv:1110.3193)

Li X., Mandelbaum R., 2023, *MNRAS*, 521, 4904

Li X., Katayama N., Oguri M., More S., 2018, *MNRAS*, 481, 4445

Li X., et al., 2022a, *PASJ*, 74, 421

Li X., Li Y., Massey R., 2022b, *MNRAS*, 511, 4850

Li S.-S., et al., 2023, *A&A*, 670, A100

Li X., Mandelbaum R., Jarvis M., Li Y., Park A., Zhang T., 2024, *MNRAS*, 527, 10388

MacCrann N., et al., 2022, *MNRAS*, 509, 3371

Mandelbaum R., 2018, *ARA&A*, 56, 393

Mandelbaum R., et al., 2018a, *MNRAS*, 481, 3170

Mandelbaum R., et al., 2018b, *MNRAS*, 481, 3170

Massey R., Refregier A., 2005, *MNRAS*, 363, 197

Massey R., et al., 2007, *MNRAS*, 376, 13

Massey R., et al., 2013, *MNRAS*, 429, 661

Moffat A. F. J., 1969, *A&A*, 3, 455

Pujol A., Kilbinger M., Sureau F., Bobin J., 2019, *A&A*, 621, A2

Refregier A., 2003, *MNRAS*, 338, 35

Refregier A., Kacprzak T., Amara A., Bridle S., Rowe B., 2012, *MNRAS*, 425, 1951

Rowe B. T. P., et al., 2015, *Astronomy and Computing*, 10, 121

Sanchez J., Mendoza I., Kirkby D. P., Burchat P. R., LSST Dark Energy Science Collaboration 2021, *JCAP*, 2021, 043

Sheldon E. S., Huff E. M., 2017, *ApJ*, 841, 24

Sheldon E. S., Becker M. R., MacCrann N., Jarvis M., 2020, *ApJ*, 902, 138

Sheldon E. S., Becker M. R., Jarvis M., Armstrong R., LSST Dark Energy Science Collaboration 2023, *The Open Journal of Astrophysics*, 6, 17

Spergel D., et al., 2015, preprint, (arXiv:1503.03757)

The LSST Dark Energy Science Collaboration et al., 2018, arXiv e-prints, p. arXiv:1809.01669

Virtanen P., et al., 2020, *Nature Methods*, 17, 261

Zhang J., 2008, *MNRAS*, 383, 113

Zhang Z., Sheldon E. S., Becker M. R., 2023, *The Open Journal of Astrophysics*, 6, 16

conda-forge community 2021, The conda-forge Project: Community-based Software Distribution Built on the conda Package Format and Ecosystem, doi:10.5281/zenodo.4774217, <https://doi.org/10.5281/zenodo.4774217>

von Kármán T., 1948, *Proceedings of the National Academy of Science*, 34, 530

## APPENDIX A: PIPELINE

We briefly summarize the pipeline for ensemble shear estimation as follows:

- (i) The center of every pixel is considered as a candidate of galaxy.
- (ii) Apply a binary pixel mask to the image to set regions near bright stars to zero.
- (iii) Add a pure noise image with the same statistical properties, but rotated by  $90^\circ$ , to the image.
- (iv) Deconvolve the PSF and convolve the image with a Gaussian to calculate the peak detection modes ( $\tilde{q}_i$ ) for each pixel and compute the detection weight ( $\tilde{w}_d$ ).
- (v) Select the peak pixels with  $\tilde{w}_d > 0$  as peaks of detected sources, and use them as origins for the measurements below.
- (vi) Create a continuous smoothed version of the binary pixel mask from step (i) and eliminate detections at pixels that fall above a threshold in this smoothed mask.
- (vii) Measure the shapelet modes ( $\tilde{M}_{nm}$ ), their shear responses, and the shear responses of the peak detection modes;
- (viii) Compute the nonlinear observables, including selection weight ( $\tilde{w}_s$ ) and ellipticity ( $\tilde{\epsilon}_{1,2}$ );
- (ix) Select the source with  $w_s > 0$  to compute the weighted ellipticity  $e_{1,2}$ .
- (x) Measure the measurement errors of shapelet modes ( $\delta M'_{nm}$ ) and the peak detection modes ( $\delta q'_i$ ) and their shear responses from the pure noise image at the position of the detected peaks.
- (xi) Compute the shear responses of the weighted ellipticity following equation (41).
- (xii) Estimate shear with equation (42).

## APPENDIX B: NOISE RESPONSE

In Section 2.2.2, we demonstrate our ability to add an additional layer of noise, identical in statistics to the original noise after rotating by  $90^\circ$  counterclockwise, to an image and subsequently derive the linear shear response from the galaxy image with two layers of noise. Since the shear distortion affects only the galaxy and not the noise, the estimated shear response is calculated by subtracting the effective shear responses of the two noise images from the overall shear response of the noisy image.

In this appendix, we validate the claim made in equation (40) that the expected effective shear responses of each noise image are identical:

$$\begin{aligned} & \left\langle \partial_i e_1(\boldsymbol{\nu} + \delta\boldsymbol{\nu} + \delta\boldsymbol{\nu}') \Big|_{\gamma=0} \delta\nu'_{1i} \right\rangle \\ &= \left\langle \partial_i e_1(\boldsymbol{\nu} + \delta\boldsymbol{\nu} + \delta\boldsymbol{\nu}') \Big|_{\gamma=0} \delta\nu_{1i} \right\rangle, \end{aligned} \quad (\text{B1})$$

where  $\partial_i e_1$  refers to the  $i$ th element of the gradient vector of  $e_1$ .  $\delta\boldsymbol{\nu}$  is the linear observable vector measured from the original noise image.  $\delta\boldsymbol{\nu}'$  is the linear observable vector measured from the additional noise image.

We start from the left-hand side:

$$\left\langle \partial_i e_1(\boldsymbol{\nu} + \delta\boldsymbol{\nu} + \delta\boldsymbol{\nu}') \Big|_{\gamma=0} \delta\nu'_{1i} \right\rangle, \quad (\text{B2})$$

which remains unchanged if we rotate the galaxies and the

two levels of image noises all together by  $90^\circ$ . To prove equation (40), we rotate the galaxies by  $90^\circ$  clockwise and recompute the left-hand side. This is equivalent to rotating both the original image noise and the additional image noise by  $90^\circ$  counterclockwise, while keeping the galaxies unchanged. Since the shapes of galaxies are isotropically oriented and their positions are randomly distributed, the estimation from the rotated galaxy sample remains the same. Consequently, we have

$$\begin{aligned} & \left\langle \partial_i e_1(\boldsymbol{\nu} + \delta\boldsymbol{\nu} + \delta\boldsymbol{\nu}') \Big|_{\gamma=0} \delta\nu'_{;1i} \right\rangle \\ &= \left\langle \partial_i e_1(\boldsymbol{\nu} + \delta\boldsymbol{\nu}' + \delta\boldsymbol{\nu}'') \Big|_{\gamma=0} \delta\nu''_{;1i} \right\rangle, \end{aligned} \quad (\text{B3})$$

where  $\delta\boldsymbol{\nu}''$  has the same statistics with the original noise after being rotated by  $180^\circ$  counterclockwise. To be more specific, the rotation transforms  $\delta\boldsymbol{\nu}$  to  $\delta\boldsymbol{\nu}'$  and transforms  $\delta\boldsymbol{\nu}'$  to  $\delta\boldsymbol{\nu}''$ . We note that for homogeneous noise, rotating the coordinate by  $180^\circ$  does not change the statistics of the noise field; therefore, we can replace  $\delta\boldsymbol{\nu}''$  with  $\delta\boldsymbol{\nu}$  in the last equation and obtain equation (40).